Smoothed particle hydrodynamics for root growth mechanics

Matthias Mimault, Mariya Ptashnyk, George Bassel, Lionel Dupuy

Smoothed particle hydrodynamics for root growth mechanics

Matthias Mimault[a], Mariya Ptashnyk[b], George W. Bassel[c], Lionel X. Dupuy[a,*]

[a] *The James Hutton Institute*
[b] *Heriot-Watt University*
[c] *University of Birmingham*

Abstract

A major challenge of plant developmental biology is to understand how cells grow during the formation of an organ. To date, it has proved difficult to develop computational models of entire organs at cellular resolution and, as a result, the testing of hypotheses on the biophysics of self-organisation is currently limited.

Here, we formulate a model for plant tissue growth in an SPH framework. The framework identifies the SPH particle with individual cells in a tissue, but the tissue growth is performed at the macroscopic level using SPH approximations. Plant tissue is represented as an anisotropic poro-elastic material where turgor pressure deforms the cell walls and biosynthesis and cell division control the density of the tissue.

The performance of the model is evaluated through a series of tests and benchmarks. Results demonstrate good stability and convergence of simulations as well as readiness of the technique for more complex biological problems.

Keywords: anisotropic material, cell division, DualSPHysics, root growth model, smoothed particle hydrodynamics.

1. Introduction

Growth in plant tissues results from processes taking place at different scales. At the macroscopic scale, the environment influences growth through water

*Corresponding author
Email address: lionel.dupuy@hutton.ac.uk (Lionel X. Dupuy)

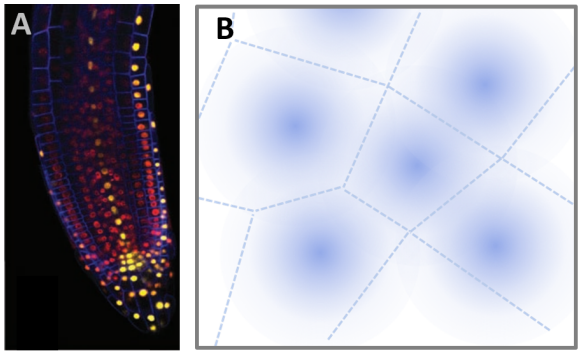

Figure 1: (A) Root apical meristem of the plant Arabidopsis thaliana expressing fluorescent proteins marking the activity of the cell in the nucleus (red / yellow gradient) and the boundaries of the cell walls (blue) [36]. The picture illustrates the importance of the gradient in the cellular activity on growth and the developmental response of the organ. (B) In our framework, each cell is represented by an SPH particle.

and nutrient within the soil matrix, the mechanical properties of the soil or the gradient of light through the canopy. However the understanding of plant responses to the environment at macroscopic scale remains a challenge. Tissues and organs are ensembles of microscopic cells which individual actions integrate into an emergent behaviour. The cells carry the genetic information, mediate the flow of nutrients, and inhibit or facilitate the elongation of cell walls, and growth and development results from the coordinated actions of these millions of cellular interactions. Microscopy techniques now allow direct observation of the growth of roots and their anatomy in substrates that reproduce natural conditions [30, 32, 40], and it is our ability to simulate organ at cellular resolution that remains limited.

The Smoothed Particle Hydrodynamics is a particle-based method, used to solve macroscopic problems with an unstructured distribution of particles as integration points. It has been developped by Gingold and Monaghan [44] and Lucy [68], and is known for the simplicity and robustness of kernel integration. It has been used to simulate incompressible and viscous fluid flows, problems in astrophysics, and large deformations of solid materials [74, 63, 72, 98]. Several codes have been developed to solve scientific and industrial problems [20, 77, 80, 87], and among them DualSPHysics has revealed most suitable for our model because of its flexibility, its performances, and the strong activity of its developer community [25].

SPH provides a natural framework for multi-scale problems, with a strong potential for applications in biology where requirements include integration of

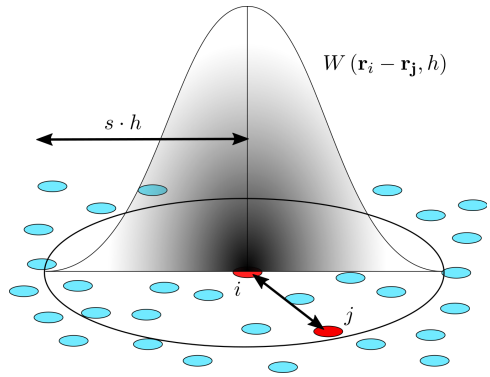

Figure 2: Schematic representation of an SHP kernel centred on particle a, computing the relation between particle i and j with the kernel W of smoothing length h. The radius of the smoothing kernel is a multiple s of the smoothing length.

multiple processes in complex and dynamic geometries. Its meshless formulation proved suitable to large deformation problems such as those found in ballistics, geo-disasters and tissue behaviour [2, 26, 39, 51, 49, 52, 56, 83, 89]. The theoretical for poro-elasticity has been developped [17, 75, 76, 93] which facilitates development of plant tissue mechanics, and growth modelled as particles of variable mass has already been used in problems of accretion in black holes or for the particle treatment in influx/outflux boundaries [15, 24, 37, 96]. Finally, the cell division is analogous to particle splitting techniques that have been studied extensively [23, 57, 50, 62, 64, 91, 90].
Here, we propose a framework that links experimental data to computational modelling, based on the SPH method. It describes the growth of plant tissue at cellular level by identifying the cells to the numerical particles (Fig. 1). The paper first presents the equations of the model and their SPH formulation in Section 2 and in Section 3 we describe the implementation of the model in DualSPHysics. The model is evaluated in Section 4 and 5 with several numerical tests, and the results are reviewed in Section 6, along with the future development of the model in a global image processing pipeline.

2. SPH formulation of the model

2.1. Basics of SPH

Smoothed Particles Hydrodynamics is a particle-based method that uses local interpolation to approximate continuous field quantities. SPH is based on the following identity to express any spatial function $f(\mathbf{r})$

$$f(\mathbf{r}) = \int_{\Omega} f(\mathbf{r}')\delta(\mathbf{r} - \mathbf{r}')\mathrm{d}\mathbf{r}', \tag{1}$$

where δ is the Delta Dirac. As δ is not differentiable, it is approximated by a smooth function called *integration kernel* to interpolate the continuous field variables. The domain of integration Ω is represented by a discrete set of particles, where the elementary volume of a particle i is $\frac{m_i}{\rho_i}$ with m_i being the mass and ρ_i the density of the particle. Hence, the interpolated value of a function f at particle i, located at $\mathbf{r}_i$ can be expressed as

$$f(\mathbf{r}_i) = \langle f \rangle_i = \sum_j \frac{m_j}{\rho_j} W(\mathbf{r_i} - \mathbf{r_j}, h), \tag{2}$$

where j is the index of neighbouring particles, $W(r, h)$ is the integration kernel, with a compact support of radius $s \cdot h$, $s \in \mathbb{R}^+$ and the regularisation length h is called the *smoothing length* (Fig, 2). The brackets represent the evaluation of the function at the centre of the particle i.
In a similar way, the gradient of a function f reads

$$\langle \nabla f \rangle_i = \sum_j \frac{m_j}{\rho_j} \nabla W(\mathbf{r_i} - \mathbf{r_j}, h). \tag{3}$$

2.2. Conservation of mass and momentum

A solid body of root tissue is modelled in a three dimensional space with cartesian coordinates (X, Y, Z), at two different scales. At the macroscopic scale (tissue level), the model describes the root in terms of partial differential equations and at the microscopic scale (cell level) we consider a particle model of interactions that identify the cells to the SPH particles. The density and momentum equations are

$$\frac{\mathrm{D}\rho}{\mathrm{D}t} = -\rho \nabla \cdot u + \gamma, \tag{4}$$

$$\frac{\mathrm{D}u}{\mathrm{D}t} = \frac{\nabla \cdot (\sigma + p)}{\rho}, \tag{5}$$

where t is the time variable, ρ the density, u the velocity vector, γ the growth, σ the stress tensor and p the pore pressure.
In the SPH formulation the terms of the equations (4)-(5) read

$$\langle \rho \nabla \cdot u \rangle_i = \sum_j m_j \left(u_j - u_i \right) \cdot \nabla_i W_{ij}, \tag{6}$$

$$\left\langle \frac{\nabla \cdot (\sigma + p)}{\rho} \right\rangle_i = \sum_j m_j \left(\frac{\sigma_i + p_i}{\rho_i^2} + \frac{\sigma_j + p_j}{\rho_j^2} + \Pi_{ij} \mathbb{I} \right) \cdot \nabla_i W_{ij} \tag{7}$$

where ρ_i, u_i and σ_i represent density, velocity and stress at particle i respectively, $\nabla_i W_{ij} = \nabla_i W(\mathbf{r}_i - \mathbf{r}_j, h)$ and Π_{ij} is the artificial viscosity term. Since the SPH uses a Lagrangian formulation, the location of a particle i is given by

$$\frac{\mathrm{D}\mathbf{r}_i}{\mathrm{D}t} = u_i. \tag{8}$$

The kernel function W is a 5-th order polynomial called the Wendland kernel [95]. It provides a good compromise between accuracy and computational efficiency, and it is well known to prevent the generation of tensile instability [61, 28]

$$W(r, h) = \begin{cases} \frac{21}{16\pi h^3} \left(1 - \frac{r}{2h}\right)^4 \left(\frac{2r}{h} + 1\right) & \text{if } 0 \leq \frac{r}{h} \leq 2, \\ 0 & \text{elsewhere.} \end{cases} \tag{9}$$

The artificial viscosity Π_{ab} has been introduced in [73] to stabilise the velocity oscillations between the particles when they get disordered. It generates numerical dissipation when particles get close to each other

$$\Pi_{ij} = \begin{cases} \frac{-\alpha_i c_0 \mu_{ij}}{\bar{\rho}_{ij}} & \text{if } (u_i - u_j) \cdot (x_i - x_j) \geq 0, \\ 0 & \text{otherwise,} \end{cases} \tag{10}$$

with usually $\alpha_i = 1$, $\bar{\rho}_{ij} = \frac{\rho_i + \rho_j}{2}$ and

$$\mu_{ij} = h \frac{(u_i - u_j) \cdot (x_i - x_j)}{|x_i - x_j|^2 + (0.1h)^2}. \tag{11}$$

The term $(0.1h)^2$ is chosen to prevent numerical divergence when particles get too close to each other.

2.3. Constitutive equations

Plant roots grow in a specific direction, due to the anisotropic properties of the cell wall matrix [8, 12, 41, 43, 78, 82]. The cell walls are composed of cellulose micro-fibrils that promote growth in the direction perpendicular to their orientation. Hence, the mechanical behaviour of the plant tissue is assumed to be transversely isotropic, where micro-fibrils are oriented in the YZ plane, promoting the growth in the X direction. For elastic deformations of a plant tissue, we consider the Hooke law $\sigma = \mathbf{C}\varepsilon$. The elasticity tensor $\mathbf{C}$ depends on five parameters, namely E_x the Young modulus in the X direction; $n = \frac{E_y}{E_x}$ the ratio between E_y the Young modulus in the YZ plane and E_x; G_{xy} the shear modulus for planes parallel to the X direction; ν_{xy} the plane reduction in the YZ plane for stress in the X direction; and ν_{yz} the plane reduction in the YZ plane for stress lying in the same plane.
Then the Hooke law in Voigt notation reads

$$\begin{pmatrix} \sigma_1 \\ \sigma_2 \\ \sigma_3 \\ \sigma_4 \\ \sigma_5 \\ \sigma_6 \end{pmatrix} = \begin{pmatrix} C_{11} & C_{12} & C_{12} & 0 & 0 & 0 \\ C_{12} & C_{22} & C_{22} - 2C_{44} & 0 & 0 & 0 \\ C_{12} & C_{22} - 2C_{44} & C_{22} & 0 & 0 & 0 \\ 0 & 0 & 0 & C_{44} & 0 & 0 \\ 0 & 0 & 0 & 0 & C_{55} & 0 \\ 0 & 0 & 0 & 0 & 0 & C_{55} \end{pmatrix} \begin{pmatrix} \varepsilon_1 \\ \varepsilon_2 \\ \varepsilon_3 \\ \varepsilon_4 \\ \varepsilon_5 \\ \varepsilon_6 \end{pmatrix} \tag{12}$$

with

$$\begin{aligned} C_{11} &= \Gamma \frac{1 - \nu_{yz}}{n}, & C_{12} &= \Gamma \nu_{xy}, \\ C_{22} &= \Gamma \frac{1 - n\nu_{xy}^2}{1 + \nu_{yz}}, & C_{44} &= \frac{E_y}{2\left(1 + \nu_{yz}\right)}, \\ C_{33} &= \Gamma \frac{1 - n\nu_{xy}^2}{1 + \nu_{yz}}, & C_{55} &= G_{xy}, \\ \Gamma &= \frac{E_y}{1 - \nu_{yz} - 2n\nu_{xy}^2}. \end{aligned} \tag{13}$$

and the compliance tensor $\mathbf{S}$ is

$$\mathbf{S} = \mathbf{C}^{-1} = \begin{pmatrix} \frac{1}{E_x} & -\frac{\nu_{xy}}{E_x} & -\frac{\nu_{xy}}{E_x} & 0 & 0 & 0 \\ -\frac{\nu_{xy}}{E_x} & \frac{1}{E_y} & -\frac{\nu_{yz}}{E_y} & 0 & 0 & 0 \\ -\frac{\nu_{xy}}{E_x} & -\frac{\nu_{yz}}{E_y} & \frac{1}{E_y} & 0 & 0 & 0 \\ 0 & 0 & 0 & \frac{2(1+\nu_{yz})}{E_y} & 0 & 0 \\ 0 & 0 & 0 & 0 & \frac{1}{G_{xy}} & 0 \\ 0 & 0 & 0 & 0 & 0 & \frac{1}{G_{xy}} \end{pmatrix}. \tag{14}$$

In the SPH formulation, the stress tensor σ is decomposed in hydrostatic pressure P and deviatoric stress τ

$$\sigma = P\mathbb{I} + \tau. \tag{15}$$

The hydrostatic pressure is assumed to depend on the tissue density and is calculated from the state equation

$$P(\rho) = K\left(\frac{\rho}{\rho_0} - 1\right) \tag{16}$$

with K the effective bulk modulus of an anisotropic material and ρ_0 the equilibrium density. It is computed from the compliance tensor [38]

$$K = \frac{1}{w^t \mathbf{S} w} \tag{17}$$

where $w = (1, 1, 1, 0, 0, 0)$.
The deviatoric stress is defined as

$$\tau = \mathbf{P}\sigma = \mathbf{P}\mathbf{C}\varepsilon \tag{18}$$

with $\mathbf{P} = \mathbb{I} - \frac{1}{3}ww^t$.
To take into account large deformations, the rate of deviatoric stress $\frac{\mathrm{D}\tau}{\mathrm{D}t}$ is computed independently from the material frame of reference using the Jaumann derivative

$$\frac{\mathrm{D}\tau}{\mathrm{D}t} = \mathbf{P}\mathbf{C}\dot{\varepsilon} + \omega\tau - \tau\omega \tag{19}$$

where $\dot{\varepsilon} = \frac{1}{2}\left(\nabla u + \nabla u^T\right)$ is the rate of the strain tensor and $\omega = \frac{1}{2}\left(\nabla u - \nabla u^T\right)$ the spin tensor, see [46] for more details. The velocity gradient ∇u is obtained by the following first order approximation at particle i

$$\langle \nabla u \rangle_i = \sum_j \frac{m_j}{\rho_j} \left(u_j - u_i\right) \nabla_i W_{ij}. \tag{20}$$

Using (19), it leads to the SPH formulations of the rate of deviatoric stress

$$\left\langle \frac{\mathrm{D}\tau}{\mathrm{D}t} \right\rangle_i = \mathbf{PC}\dot{\varepsilon}_i + \omega_i \tau_i - \tau_i \omega_i. \tag{21}$$

Therefore, the value of stress at particle i is

$$\sigma_i = P(\rho_i)\mathbb{I} + \tau_i. \tag{22}$$

2.4. Turgor pressure

Plant cells have plasma membranes that are permeable to fluids of different concentration. It creates an osmotic pressure inside the cell, called the turgor pressure [9, 100]. The model is formulated in a poro-elastic framework, where the cell wall matrix is the solid phase and the turgor pressure is associated to the pore pressure [22, 84].

$$p_i = p_0 \mathbb{I}. \tag{23}$$

Pore pressure is kept positive to prevent any shrinking of the plant tissue.

2.5. Biosynthesis

During the growth of a tissue, the cells increase in mass, mainly because of water influx and thickening of walls through acumulation of pectins and polysacharrides [21, 41]. The later process prevents the thinning of cell walls and the weakening of elongating tissue. Biomass deposition is modelled as a densification process, expressed as a function of the density ρ_i and the growth rate λ_g [3, 45, 55, 59].

$$\gamma\left(\rho_i\right) = \lambda_g \left(\frac{\rho_0}{\rho_i} - 1\right). \tag{24}$$

Similar laws have been documented for instance in bone growth [45, 55]. The densification model accounts for a range of processes. First, the relationship incorporates changes in cell mass due to either biological (turgor, cell softening) and physical (drying of tissue) processes.

It is worth noting that the formulation is reversible and therefore can lead to contraction of the tissue. This form of growth is a physical reality when adaptation to external forces is not fast enough, for example when a root reaches a physical barrier. In this case, elongation zones were shown to exhibit contraction [14]. When deviations from equilibrium density are small, the densification rate is proportional to the difference in tissue density which makes the relationship symmetric. This assumption cannot be confirmed experimentally because cell mass cannot be measured at this resolution. It is however a reasonable model hypothesis considering that water dominates the mass of the cell.

The densification mechanism has also a second important role in growth. Because density is related to pressure (16), it is linked to the permanent extension of the tissue. Therefore the growth rate λ_g controls indirectly the relaxation of the tissue's elasticity. Although the model is not directly formalised in the viscoplastic framework, it implements a relaxation mechanism that is stable and requires a single parameter. This is a reasonable approach considering that it is not possible to characterize the visco-plastic parameters of cells live and *in situ*.

2.6. Cell division

Cell division is a fundamental mechanism through which plants maintain an organised cellular architecture and achieve highly specialised functions. Control of the cell architecture is achieved through cell expansion, but also through the frequency and the location of the new cell walls appearance. To maintain a distribution of SPH particles that matches the cells of natural tissues, it is therefore essential to derive a cell division model that mimics the patterns observed in natural systems. A cell division model can be decomposed into three components.

(1) The cell division checkpoint. During its lifetime, a cell passes through a series of checkpoints that ultimately triggers the division. There is no widely accepted model for cell division in plants because the biological mechanisms involved are complex and the mathematical formulations are still debated. However microscopy observations indicate that the sensing of size and geometry of the cell is essential to divide at the right time and place. For this reason, mathematical models have often used cell size but also cell type or age as triggers for cell division [32, 54, 67, 97]. In our model, we

chose cell division to be triggered by particle mass. The division of a particle occurs when the particle mass reaches a threshold size $\bar{m}$. Since the density of the tissue is maintained at values close to equilibirum due to biosynthesis, the mass criterion is equivalent to a size criterion, and this ultimately controls the particle size distribution at steady state.

(2) The geometry of the division. The geometric rules underlying the placement of new cell walls are also intensely debated. There are no widely accepted rules for the placement of new cell walls during division, but Errera's principle, whereby the division minimises the surface area of daughter cells of identical volume, is commonly used [19, 60, 66]. It has inspired many recent models [10, 34, 86]. Here, the orientation of the division is a normalised vector $\mathbf{d}_i \in \mathbb{R}^3$ that depends on the principal axes of deformation of the tissue. The position of the new particles is determined along $\mathbf{d}_i$, and Δx defines the distance from the centre of the mother cell where the new particles are placed. It is obtained through a backward volume formula,

$$\Delta x_i = \frac{1}{2}\mathrm{vol}^{-1}\left(\frac{m_i}{\rho_i}\right). \tag{25}$$

Here the volume calculation can be defined as either a rectangular brick shape for instance in the case of uniaxial expansion or spherical in the case of isotropic expansion. The locations $\mathbf{r}^*$ of the daughter particles are

$$\begin{aligned} \mathbf{r}_i^* &= \mathbf{r}_i + \mathbf{d}_i \Delta x_i, \\ \mathbf{r}_{i'}^* &= \mathbf{r}_i - \mathbf{d}_i \Delta x_i. \end{aligned} \tag{26}$$

Assumptions on cell shapes are required because deformation of individual cell shapes are not available during computation. The resulting division model approaches Errera's rule because cutting the length along the main axis of a cell produces the smallest cross section, and the symmetry of the placement of particles ensures daughter cells have equal size and volume.

(3) The kinematics of the division. Since a cell division is the formation of a rigid wall inside a cell, the daughter cells inherit naturally the velocity of their mother (Fig. 3). The daughter cells are labelled i and $i' = N + 1$, where N is the total number of particles before the division.

3. Implementation

The model is implemented using the numerical code DualSPHysics, based on C++, OpenMP and CUDA. Initially designed to simulate fluid dynamics,

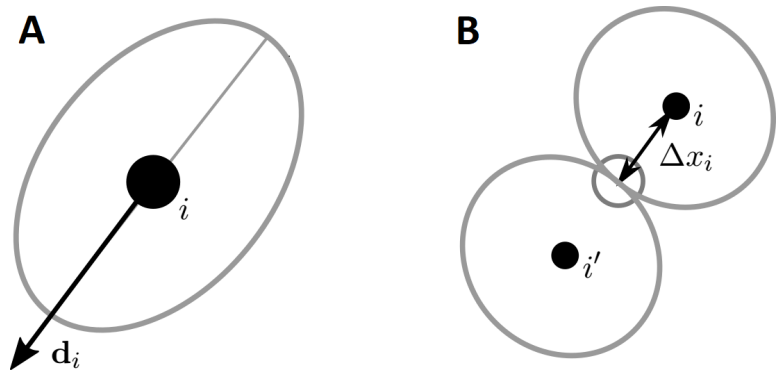

Figure 3: Schematic representation of the cell division procedure of a particle i. The particle divides along the direction $\mathbf{d}_i$ (A) and the daughter particles are set apart from each other at a distance equal to Δx_i (B).

it is highly customisable, well maintained and proposes good performances in parallel computations [25].

The numerical integration of the dynamics is performed as follow. First the node computes the poro-elastic deformation in response to the pore pressure. In a second step, the variation of mass due to the growth is calculated. Finally the cell division procedure checks for particles that reach the threshold mass and performs their division.

3.1. Time integration

The integration of the quantities at particle i is based on a Verlet scheme [94]. It proposes good stability for a low computational overhead. The numerical integration is based on two time steps. The time step for the computation of the poro-elastic deformation reads from (6), (7) and (21)

$$\begin{aligned}
\mathbf{r}_i^{n+1} &= \mathbf{r}_i^{n-1} + \Delta t u_i^n + \frac{(\Delta t)^2}{2} \left\langle \frac{\nabla \cdot (\sigma + p)}{\rho} \right\rangle_i^n , \\
u_i^{n+1} &= u_i^{n-1} + 2\Delta t \left\langle \frac{\nabla \cdot (\sigma + p)}{\rho} \right\rangle_i^n , \\
\tau_i^{n+1} &= \tau_i^{n-1} + 2\Delta t \left\langle \frac{\mathrm{D}\tau}{\mathrm{D}t} \right\rangle_i^n , \\
\hat{\rho}_i^n &= \rho_i^{n-1} - 2\Delta t \left\langle \rho \nabla \cdot u \right\rangle_i^n ,
\end{aligned} \tag{27}$$

where the superscript n denotes the time step, the brackets $\langle \cdot \rangle_i$ the SPH approximation of the quantity at particle i and $\hat{\rho}$ is the intermediate density related to only deformation.

The stability condition is given by $\Delta t = \lambda_{\mathrm{CFL}} \min\{\Delta t_f, \Delta t_{cv}\}$ where

$$\Delta t_f = \min_i \left\{ \sqrt{\frac{h}{\|\mathbf{f}_i\|}} \right\} \text{ and } \Delta t_{cv} = \min_i \left\{ \frac{h}{c_0 + \max_j \{\mu_{ij}\}} \right\}, \tag{28}$$

with λ_{CFL} is a constant between 0 and 1 and $\mathbf{f}_i = \left\langle \frac{\nabla\cdot(\sigma+p)}{\rho} \right\rangle_i$. The version implemented in DualSPHysics includes a correction for the decoupling of the computed quantities that replaces the integration step by an explicit Euler step every certain number of time steps, noted here N_{Verlet}.

3.2. Growth

The growth process is separated in two distinct steps with the mass increase occurring separately from the deformation. It is assumed to happen at constant volume, so the particle mass and density are updated according to (24), with $\gamma_i^n = \gamma(\hat{\rho}_i^n)$

$$m_i^{n+1} = m_i^{n-1}\left(1 - 2\Delta t \frac{\gamma_i^n}{\hat{\rho}_i^n}\right), \tag{29}$$

$$\rho_i^{n+1} = \hat{\rho}_i^n + 2\Delta\gamma^n. \tag{30}$$

3.3. Cell division

The cell division is implemented as a source of particles. The daughter particles are composed of the original particle and a duplicated one, with a shifted position and a mass divided by two. First, the cell division procedure checks and marks the particles that satisfy the division rule

$$m_i > \bar{m} = \lambda_m m_0, \tag{31}$$

where m_0 is the initial mass of the particles and λ_m a scaling parameter. Then the memory arrays are extended and filled with a copy of the duplicated particles data, except for the mass, which is divided by two, and the position, which is updated according to the backward volume formula (25).

3.4. Smoothing length

The smoothing length h is a constant defined as follows

$$h = 2\sqrt[3]{\frac{\bar{m}}{\rho_0}}. \tag{32}$$

It assumes that the smoothing length is proportional to the side of a cube centred on the particle, at the maximal volume it can reach before cell division. Usually, when the mass of a particle varies, the smoothing length follows to prevent any disparity in the density evaluation. Here however, the density is assumed to be constant and the solid structure stable, it is sufficient to ensure the capture of the influence of the biggest particles.

3.5. Boundary conditions

The surface of a root can be highly deformed, as the result of a trade-off between the inner pressure and the resistance of the soil. The surface particles are left free and the formulation (4) prevents the apparition of boundary errors in the density. This setting describes the free growth of a part of plant root in a nutritive liquid that has negligible momentum effects.

4. Numerical tests

The features and performances of the model are tested in several configurations. The domains are filled with particles distributed on a uniform Cartesian lattice with an initial spacing $\Delta x_{i,0}$. The initial mass of a particle i is

$$m_{i,0} = \Delta x_{i,0}^3 \rho_0, \tag{33}$$

and ρ_0 is the initial density.

First the poro-elastic model is evaluated in the isotropic and anisotropic cases and compared to analytical predictions for several particle discretisations. Then we test the growth process and compare the results to analytical predictions. The tests are performed in three dimensions with parameters typically used in porous materials using the **L1**-norm of the density and deformation field along with the **L2**-norm of the error. They are computed as

$$\|f\|_{\mathbf{L1}} = \sum_i \frac{v_i}{V} |f_i|, \tag{34}$$

$$\|f - \bar{f}\|_{\mathbf{L2}} = \sqrt{\sum_i \frac{v_i}{V} \left(f_i - \bar{f}(\mathbf{r}_i)\right)^2}, \tag{35}$$

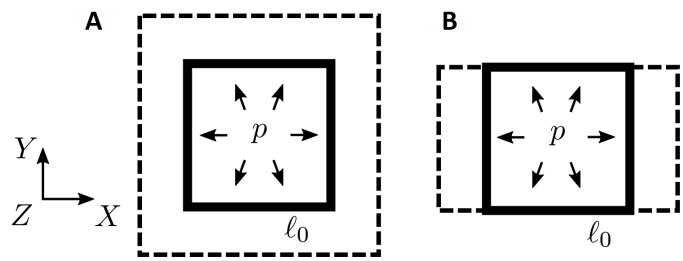

Figure 4: Schematic representation of the isotropic (A) and anisotropic (B) deformation of a cube of length ℓ_0 under pore pressure p. To reach a new density equilibrium, the tissue body has to deform.

where f is a field quantity, f_i is the evaluation of this function at particle i, $\bar{f}$ its exact evaluation, $v_i = \frac{m_i}{\rho_i}$ is the local volume, $V = \sum_i v_i$ is the total volume, and $\mathbf{r}_i$ is the position of particle i.

4.1. Poro-elastic deformation

A cube of side length $\ell_0 = 1\,\mathrm{m}$ with the centre localised at $(0,0,0)$ and at equilibrium density ρ_0 is deformed under a pore pressure $p = 100\,\mathrm{MPa}$ (Fig. 4, A). The material properties are

$$\begin{aligned} K &= 12500\,\mathrm{MPa}, \quad \rho_0 = 1000\,\mathrm{kg\,m^{-3}}, \\ E &= 15000\,\mathrm{MPa}, \quad \nu = 0.3. \end{aligned} \tag{36}$$

The expected values of the equilibrium density and deformation are

$$\bar{\rho} = \rho_0 \left(1 - \frac{p}{K}\right) = 992\,\mathrm{kg.m^{-3}}, \tag{37}$$

$$\bar{\varepsilon}_x = \bar{\varepsilon}_y = \bar{\varepsilon}_z = \frac{1-2\nu}{E} p = 2.667 \times 10^{-3}. \tag{38}$$

The numerical simulations are performed for space steps from $\Delta x_{i,0} = 0.05$ to $0.0125\,\mathrm{m}$ with the following numerical parameters

$$\begin{aligned} T &= 10\,\mathrm{s}, \qquad \mathrm{CFL} = 0.1, \\ h &= 2\Delta x_{i,0}, \quad \mathrm{N_{Verlet}} = 5. \end{aligned} \tag{39}$$

The deformation $\varepsilon_{x,i}$ is computed for each particle i with the current position x_i compared to the initial position $x_{i,0}$

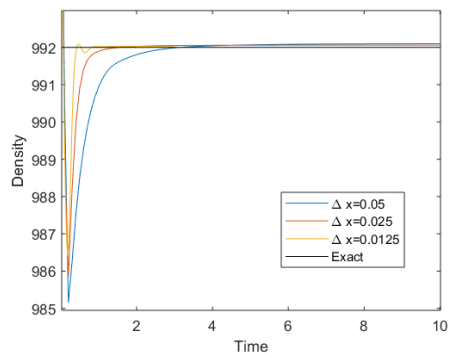

Figure 5: Evolution of the density as a function of SPH resolution. Computer density is compared to theoretical values $\bar{\rho}$.

$\Delta x_{i,0}$	$\|\rho\|_{\mathbf{L1}}$	$\|\rho - \bar{\rho}\|_{\mathbf{L2}}$
0.05	992.0944	6.2682×10^{-3}
0.025	992.0076	1.1571×10^{-5}
0.0125	992.0037	4.8360×10^{-6}

Table 1: Estimation of density with parameters defined in (36).

$$\varepsilon_{x,i} = \frac{x_i}{x_{i,0}} - 1. \tag{40}$$

The evolution of density displays a fluctuation at the beginning for each simulatio (Fig. 5). The application of the pore pressure to a solid at rest generates a shock-wave before the density reaches steady state. The magnitude of the wave reduces as the space step $\Delta x_{i,0}$ decreases. The density reaches a steady state comparable to the expected values of ρ and ε_x. These results (Tab. 1 and Tab. 2) show a close match between numerical and theoretical values, and the **L2** error decreases monotonically.

Next we perform numerical simulations using anisotropic properties of cell walls materials. Growth is facilitated in the X direction with a minimal deformation in the YZ plane. The material properties are

$$\begin{aligned} &K = 1192.7030\,\mathrm{MPa}, && \rho_0 = 1000\,\mathrm{kg\,m^{-3}}, \\ &E_x = 1020\,\mathrm{MPa}, && T = 10\,\mathrm{s}, \\ &E_y = 15000\,\mathrm{MPa}, && p = 10\,\mathrm{MPa}, \\ &\nu_{xy} = 0.06, && \nu_{yz} = 0.3. \end{aligned} \tag{41}$$

$\Delta x_{i,0}$	$\|\varepsilon_x\|_{\mathbf{L1}}$	$\|\varepsilon_y\|_{\mathbf{L1}}$	$\|\varepsilon_z\|_{\mathbf{L1}}$
0.05	2.9789×10^{-3}	2.9789×10^{-3}	2.9789×10^{-3}
0.025	2.9258×10^{-3}	2.9260×10^{-3}	2.9258×10^{-3}
0.0125	2.7173×10^{-3}	2.7173×10^{-3}	2.7173×10^{-3}
$\Delta x_{i,0}$	$\|\varepsilon_x - \bar{\varepsilon}_x\|_{\mathbf{L2}}$	$\|\varepsilon_y - \bar{\varepsilon}_y\|_{\mathbf{L2}}$	$\|\varepsilon_z - \bar{\varepsilon}_z\|_{\mathbf{L2}}$
0.05	8.2853×10^{-6}	8.2853×10^{-6}	8.2853×10^{-6}
0.025	2.3755×10^{-6}	2.3783×10^{-6}	2.3755×10^{-6}
0.0125	1.1298×10^{-7}	1.1302×10^{-7}	1.1302×10^{-7}

Table 2: Estimation of components of the strain tensor in the isotropic case (36).

$\Delta x_{i,0}$	$\|\rho\|_{\mathbf{L1}}$	$\|\rho - \bar{\rho}\|_{\mathbf{L2}}$
0.05	991.5750	5.9130×10^{-5}
0.025	991.5837	2.3162×10^{-5}
0.0125	991.6056	9.4279×10^{-6}

Table 3: Estimation of density in the anisotropic case (41).

Theoretical values for the strain tensor and tissue density of the deformed solid are:

$$\begin{aligned} \bar{\rho} &= 991.6157\,\mathrm{kg\,m^{-3}}, \\ \bar{\varepsilon}_x &= 8.6274 \times 10^{-3}, \\ \bar{\varepsilon}_y &= -1.12573 \times 10^{-4}. \end{aligned} \tag{42}$$

Those values describe a growth facilitated in the X direction, with the deformation in the Y and Z direction being an order of magnitude smaller than the elongation in the X direction.
Results are similar to the the previous test (Tab. 3 and 4) and show there is good agreement between numerical and predicted density and deformation. The change of material behaviour results in the uniaxial elongation of the initial domain.

4.2. Anisotropic growth

Growth is then considered in an anisotropic configuration (Fig.6, A). The pore pressure is imposed to a bounded domain corresponding to an initial cube of side length $\ell_0 = 1\,\mathrm{m}$. The material properties are defined as in (41) with

$$\lambda_g = 200\,\mathrm{kg} \tag{43}$$

$\Delta x_{i,0}$	$\|\varepsilon_x\|_{\mathbf{L1}}$	$\|\varepsilon_y\|_{\mathbf{L1}}$	$\|\varepsilon_z\|_{\mathbf{L1}}$
0.05	1.0703×10^{-2}	-1.3910×10^{-4}	-1.3970×10^{-4}
0.025	9.5661×10^{-3}	-1.3394×10^{-4}	-1.3394×10^{-4}
0.0125	9.2731×10^{-3}	-1.3102×10^{-4}	-1.3102×10^{-4}
$\Delta x_{i,0}$	$\|\varepsilon_x - \bar{\varepsilon}_x\|_{\mathbf{L2}}$	$\|\varepsilon_y - \bar{\varepsilon}_y\|_{\mathbf{L2}}$	$\|\varepsilon_z - \bar{\varepsilon}_z\|_{\mathbf{L2}}$
0.05	5.4356×10^{-5}	3.7688×10^{-6}	3.7617×10^{-6}
0.025	6.7148×10^{-6}	5.7906×10^{-7}	5.7808×10^{-7}
0.0125	9.3215×10^{-7}	1.1831×10^{-7}	1.1853×10^{-7}

Table 4: Estimation of the component of the strain tensor in the anisotropic case (41).

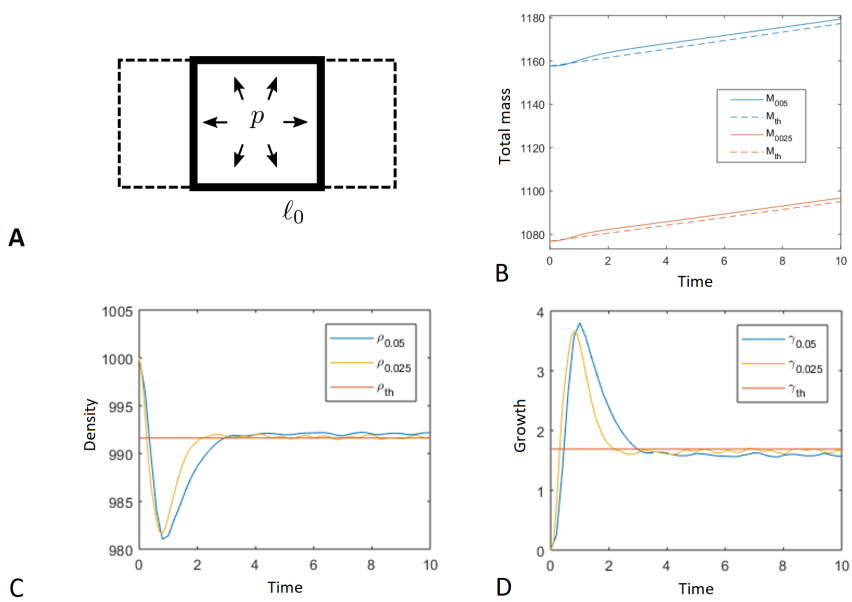

Figure 6: Schematic representation of the growth of a cube of initial length ℓ_0 under a pore pressure p. Associated evolution of mass (B), density (C) and growth rate (D). The deformation is maintained by the imbalance between the turgor pressure and the assimilation of biomass.

$\Delta x_{i,0}$	M_0	V_0
0.05	1157.625	1.1576
0.025	1076.896	1.0769

Table 5: Values of M_0 and V_0 for each discretisation in the anisotropic case (43).

We evaluate the growth rate and the total mass against their predicted values

$$\bar{\gamma} = \lambda_g \left(\frac{\rho_0}{\bar{\rho}} - 1 \right) = 1.6910\,\mathrm{kg\,m^{-3}\,s^{-1}}, \tag{44}$$

$$\overline{M}(t) = M_0 + \bar{\gamma} V_0 t. \tag{45}$$

with $M_0 = \sum_i m_{i,0}$ and $V_0 = \sum_i \frac{m_{i,0}}{\rho_{i,0}}$.
The mesh generation algorithm in DualSPHysics causes the total mass and volume at initialisation to depend on $\Delta x_{i,0}$. Therefore the prediction is corrected with $V_0 \to 1$, with values for M_0 and V_0 for each discretisation shown in Tab. 5.
In this simulation, the total mass evolution follows the theoretical values, after the dissipation of the initial oscillation (Fig. 6, B) and the average density and growth rate evolve in line to the theoretical prediction during the simulation (Fig. 6, C-D). Growth results from the imbalance between the turgor pressure and the deposition of new cell wall material.

5. Cell division tests

Cell division can affect the results of the computations because density and spatial arrangement of SPH particles are changing with time. The nature of rearrangements are linked directly to how tissues develop. Therefore, to test the effect of cell division on SPH particles, we chose test cases for their similarity to natural growth processes. Because the morphologies and kinematics of growth involved in these cases are more complex, theoretical predictions cannot be made easily. Instead we chose to either compare the results of the simulation to cases where the cell division is absent or to analyse qualitatively the consistency of the computations.

5.1. Cell division - apical growth

First we tested the effect of cell division in the case of apical growth, which is commonly observed in root meristems. Apical growth is characterised by enhanced cell elongation with cells at the tip. Elongation is uniaxial to

the orientation of cellulose chains and growth results in the formation of cylindrical morphology observed for example in roots and stems. In these simulations, the direction of elongation is set to X, which implies that the direction of division must take place along the same axis. The material properties are as in (41) with

$$\lambda_g = 200\,\mathrm{kg.m^{-3}.s^{-1}} \quad \Delta x_{i,0} = 0.05\,\mathrm{m}. \tag{46}$$

To recover the deformation of the cell from equation (25), the cell is assumed to have the shape of a brick, and the deformation in Y and Z is considered negligible. Δx_i is recovered through a backward formula for the side of a brick. The parameters of the division at particle i are

$$\mathbf{d}_i = (1, 0, 0), \tag{47}$$

$$\Delta x_i = \frac{1}{\Delta x_{i,0}^2} \frac{m_i}{\rho_i}, \tag{48}$$

$$\lambda_m = 1.5. \tag{49}$$

Two criteria were used to assess the results of the study case. First it is important the cell division does not affect negatively the predictions of the simulation. Secondly, it is also essential that because of the large deformations, only cell division induces changes in the topology of adjacent particles. Hence, the contact between adjacent cells must be conserved during the simulation in the YZ plane.

The results of the cell division tests were compared to a growth with identical parameters but without division. The analysis of the particle distribution at $T = 350$ (Fig. 7) shows that the tissue extends consistently to a final domain several times larger than its original size. Disorganisation in the X axis is observed because of boundary effects, but the rectangular organisation in the transversal plane is conserved. Results also show that cell division does not affect negatively the stability of growth (Fig.7, C) and conservation of tissue density $\bar{\rho}$ is obtained from the simulations (Fig.7, D). As expected a linear increase in mass is obtained. These results indicate that growth is not disrupted during division and throughout the drastic increase in particle number induced by the cell division (Fig.7, E).

5.2. Effect of differential growth

The second test illustrates the formation of an isotropic outgrowth. Outgrowth are common during the development of plant organs, for example

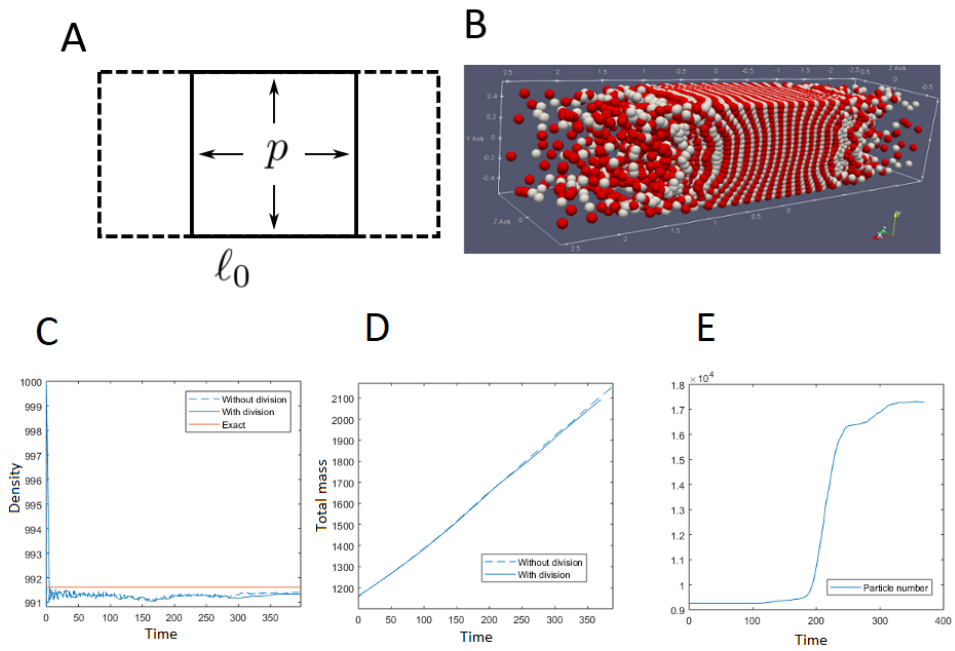

Figure 7: (A) Schematic representation of apical growth simulations. (B) Particle distribution at $T = 350$, with original particles in white shade and additional particles resulting from cell division in red. Results of the simulation show cell division does not affect the evolution of density (C), of total mass (D) with drastic increase of particle number(E).

during the formation of primordia in meristem, or during the formation of gals and tumours in response to diseases. The outgrowth here is generated from a cylindrical domain sample with non-zero pore pressure on one half of the rod (Fig. 8, A), and zero elsewhere. The increase in turgor pressure results in isotropic growth that progressively forms a bulge taking progressively a spherical shape. In this case, the orientation of cell division is given by the displacement of the mother particle. The material properties are as in (36) with

$$\begin{array}{ll} p = 0.1\,\mathrm{MPa} & T = 60\,\mathrm{s} \\ \lambda_g = 1000\,\mathrm{kg.m^{-3}.s^{-1}} & \Delta x = 0.1\,\mathrm{m} \\ & \bar{\rho} = 999.916\,\mathrm{kg.m^{-3}} \end{array} \tag{50}$$

Since growth does not expand preferentially in any direction, the shape of the cells will be approximated as a sphere. The parameters of the division model are

$$\mathbf{d}_i = \frac{u_i}{\|u_i\|}, \tag{51}$$

$$\Delta x_i = 0.3\sqrt[3]{\frac{6m_i}{\pi\rho_i}}, \tag{52}$$

$$\lambda_m = 1.5. \tag{53}$$

Results show the SPH model can be used to simulate the formation of an outgrowth (Fig. 8, B). The increase of mass and particle number tends towards a steady linear increase which is consistent with expansion (Fig. 8, C). Results also show the stability of the average density at values close to the equilibrium density ρ_0 (Fig. 8, D). The growth of mass follows a linear curve because it results from the addition of mass produced from a fixed volume of space at a constant rate, which stops when the particles enter in a region where the pore pressure is zero.

6. Discussion

In this paper, we presented a model of root growth based on Smoothed Particle Hydrodynamics. The model features the principal drivers of growth, i.e. turgor pressure, cell wall anisotropy, cell wall biosynthesis and the cell division, with SPH providing a flexible theoretical framwork for integration of microscopic and macroscopic processes.

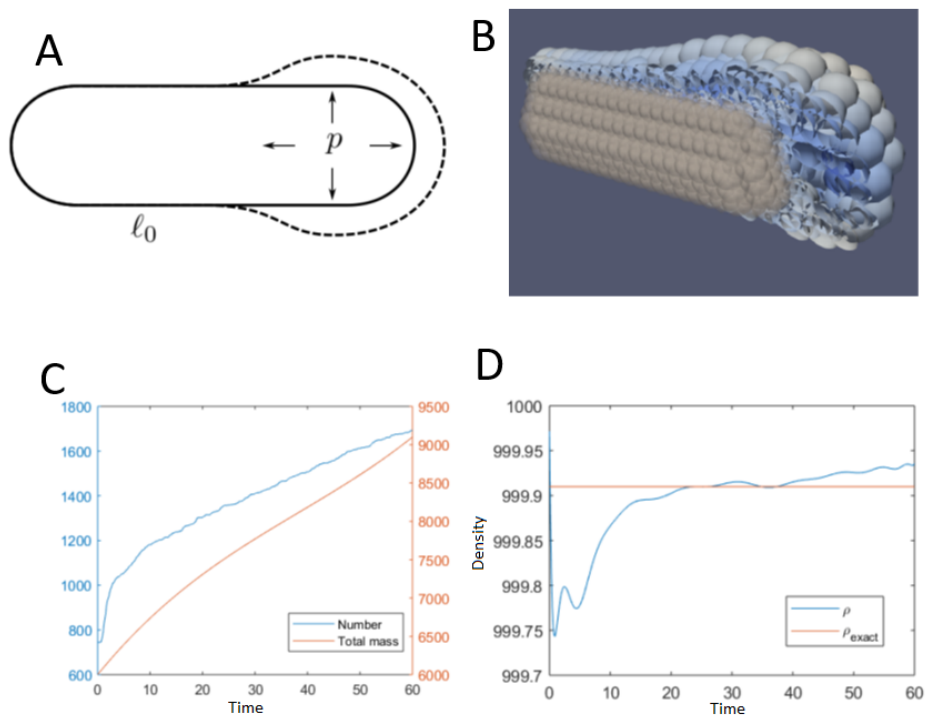

Figure 8: (A) Schematic representation of the simulation of outgrowths. (B) Particle distribution at $T = 60$. (C) Particle number and total mass evolution. (D) Density evolution.

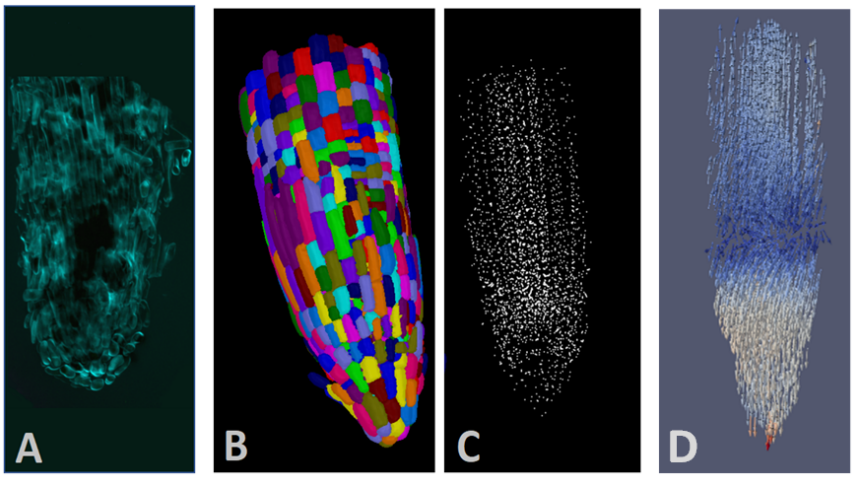

Figure 9: Pipeline for SPH computation of plant cellular development. (A) Image data obtained with 3D microscopy, courtesy Ilonka Engelhardt. (B) Segmented root apical meristem using MorphographX [6]. (C) Extraction of size and location of cells as input for SPH computation. (D) Simulation of the elongation of the root tissue

Unlike most previous continuous approaches [81, 85, 88], the individual behaviour of the cells is represented explicitely and it is possible to model the emergence of material properties from the tissue structure. Agent-based models have also been developped in the past to allow for a finer level of description, where each cell is considered as an individual with a unique behaviour. The formulation of such model is closer to reality, but analytical investigation is almost impossible [7, 11, 29, 69, 70, 92]. A way to bring together these two aspects is to formulate a multi-scale approach, combining several levels of description and allowing them to interact. Several propositions exist and among them, gene-regulated network combined to growth [4, 31, 58, 71, 27], averaging approaches through analytical homogenisation [1, 35, 65, 79, 82], and the incorporation of a representation of individual cells in a continuous formulation of tissue deformation [5, 13, 42, 48, 53, 99]. The definition of the microscopic element is crucial to elucidate fundamental processes of biological tissues development.

Kernel integration provides a robust multi-scale formulation where cells can be identified as SPH particles. Autonomous behaviour of cells is maintained at particle levels and conservation and constitutive laws describe tissue dynamics at the macroscopic level. The suitability of SPH kernels integration was confirmed by numerical tests which demonstrate the model handles ad-

equately integration of processes at microscale. Hence, this framework will be capable to handling more complex and intricate biological problems and will have application in developmental biology [83, 89].
This work aligns particularly well with ongoing efforts to develop microscopy techniques and image processing pipeline, where direct observation of roots allows to reconstruct three-dimensional visualisation [18, 30]. Data provided by such approaches can be easily incorporated into SPH simulation tools. These tools can then be used to study how cellular mechanisms contribute to the regulation of the growth of entire roots when they develop in a complex environment [33] (Fig. 9). Future work will also include the simulation of organs in contact with soil, covering tissues differentiation, and gene expression, with the coupling to other numerical methods such as the Discrete Elements Method [16, 47].

Acknowledgements

This project is supported by the consolidator fellowship from the European Research Council ERC SENSOILS-647857 and a Small Grant from the Institute of Mathematics and its Application SGS17 46. The authors thank Ilonka Engelhardt for the meristem picture (Fig. 9, A) and to Georges Bassel for the segmented root sample (Fig. 9, B).

[1] H. R. Allen and M. Ptashnyk. Mathematical Modelling of Auxin Transport in Plant Tissues: Flux meets Signalling and Growth. *arXiv preprint arXiv:1810.09161*, 2018.

[2] C. Antoci, M. Gallati, and S. Sibilla. Numerical simulation of fluid–structure interaction by sph. *Computers & Structures*, 85(11-14):879–890, 2007.

[3] G. A. Ateshian. On the theory of reactive mixtures for modeling biological growth. *Biomechanics and modeling in mechanobiology*, 6(6):423–445, 2007.

[4] L. R. Band, D. M. Wells, A. Larrieu, J. Sun, A. M. Middleton, A. P. French, G. Brunoud, E. M. Sato, M. H. Wilson, B. Peret, M. Oliva, R. Swarup, I. Sairanen, G. Parry, K. Ljung, T. Beeckman, J. M. Garibaldi, M. Estelle, M. R. Owen, K. Vissenberg, T. C. Hodgman, T. P. Pridmore, J. R. King, T. Vernoux, and M. J. Bennett. Root gravitropism is regulated by a transient lateral auxin gradient controlled by a tipping-point mechanism. *Proceedings of the National Academy of Sciences of the United States of America*, 109(12):4668–4673, 2012.

[5] M. Banwarth-Kuhn, A. Nematbakhsh, K. W. Rodriguez, S. Snipes, C. G. Rasmussen, G. V. Reddy, and M. Alber. Cell-based model of the generation and maintenance of the shape and structure of the multilayered shoot apical meristem of arabidopsis thaliana. *Bulletin of mathematical biology*, pages 1–37, 2018.

[6] P. Barbier de Reuille, A.-L. Routier-Kierzkowska, D. Kierzkowski, G. W. Bassel, T. Schüpbach, G. Tauriello, N. Bajpai, S. Strauss, A. Weber, A. Kiss, A. Burian, H. Hofhuis, A. Sapala, M. Lipowczan, M. B. Heimlicher, S. Robinson, E. M. Bayer, K. Basler, P. Koumoutsakos, A. H. K. Roeder, T. Aegerter-Wilmsen, N. Nakayama, M. Tsiantis, A. Hay, D. Kwiatkowska, I. Xenarios, C. Kuhlemeier, and R. S. Smith. MorphoGraphX: A platform for quantifying morphogenesis in 4D. *eLife*, 4:05864, 2015.

[7] D. L. Barton, S. Henkes, C. J. Weijer, and R. Sknepnek. Active vertex model for cell-resolution description of epithelial tissue mechanics. *PLoS computational biology*, 13(6):e1005569, 2017.

[8] T. I. Baskin. Anisotropic Expansion of the Plant Cell Wall. *Annual Review of Cell and Developmental Biology*, 21(1):203–222, 2005.

[9] L. Beauzamy, N. Nakayama, and A. Boudaoud. Flowers under pressure: Ins and outs of turgor regulation in development. *Annals of Botany*, 114(7):1517–1533, 2014.

[10] S. Besson and J. Dumais. Universal rule for the symmetric division of plant cells. *Proceedings of the National Academy of Sciences of the United States of America*, 108(15):6294–6299, 2011.

[11] N. Bessonov, V. Mironova, and V. Volpert. Deformable cell model and its application to growth of plant meristem. *Mathematical Modelling of Natural Phenomena*, 8(4):62–79, 2013.

[12] A. J. Bidhendi and A. Geitmann. Relating the mechanics of the primary plant cell wall to morphogenesis. *Journal of experimental botany*, 67(2):449–461, 2016.

[13] A. J. Bidhendi and A. Geitmann. Finite Element Modeling of Shape Changes in Plant Cells. *Plant Physiology*, 176(1):41–56, 2018.

[14] F. Bizet, A. G. Bengough, I. Hummel, M.-B. Bogeat-Triboulot, and L. X. Dupuy. 3d deformation field in growing plant roots reveals both

mechanical and biological responses to axial mechanical forces. *Journal of experimental botany*, 67(19):5605–5614, 2016.

[15] I. Bonnell, M. Bate, C. Clarke, and J. Pringle. Accretion and the stellar mass spectrum in small clusters. *Monthly Notices of the Royal Astronomical Society*, 285(1):201–208, 1997.

[16] F. Bourrier, F. Kneib, B. Chareyre, and T. Fourcaud. Discrete modeling of granular soils reinforcement by plant roots. *Ecological Engineering*, 61:646–657, 2013.

[17] H. Bui, R. Fukagawa, and K. Sako. A study of the matter of sph application to saturated soil problems. *arXiv preprint arXiv:1502.00495*, 2015.

[18] J. E. Burr-Hersey, S. J. Mooney, A. G. Bengough, S. Mairhofer, and K. Ritz. Developmental morphology of cover crop species exhibit contrasting behaviour to changes in soil bulk density , revealed by X-ray computed tomography. *PLoS One*, pages 1–18, 2017.

[19] C. Cadart, E. Zlotek-Zlotkiewicz, M. Le Berre, M. Piel, and H. K. Matthews. Exploring the function of cell shape and size during mitosis. *Developmental Cell*, 29(2):159–169, 2014.

[20] Z. Cao, A. Patra, M. Bursik, E. B. Pitman, and M. Jones. Plume-sph 1.0: a three-dimensional, dusty-gas volcanic plume model based on smoothed particle hydrodynamics. *Geoscientific Model Development*, 11(7):2691–2715, 2018.

[21] N. C. Carpita and D. M. Gibeaut. Structural models of primary cell walls in flowering plants: consistency of molecular structure with the physical properties of the walls during growth. *The Plant Journal*, 3(1):1–30, 1993.

[22] A. H.-D. Cheng and E. Detournay. Fundamentals of poroelasticity. *Analysis and Design Methods: Comprehensive Rock Engineering: Principles, Practice and Projects*, II:113, 2014.

[23] L. Chiron, G. Oger, M. De Leffe, and D. Le Touzé. Analysis and improvements of adaptive particle refinement (apr) through cpu time, accuracy and robustness considerations. *Journal of Computational Physics*, 354:552–575, 2018.

[24] P. J. Cossins. *The Gravitational Instability and its Role in the Evolution of Protoplanetary and Protostellar Discs.* PhD thesis, University of Leicester, 2010.

[25] A. J. C. Crespo, J. M. Domínguez, B. D. Rogers, M. Gómez-Gesteira, S. Longshaw, R. Canelas, R. Vacondio, A. Barreiro, and O. García-Feal. DualSPHysics: Open-source parallel CFD solver based on Smoothed Particle Hydrodynamics (SPH). *Computer Physics Communications*, 187:204–216, 2015.

[26] R. Das and P. W. Cleary. Evaluation of Accuracy and Stability of the Classical SPH Method Under Uniaxial Compression. *Journal of Scientific Computing*, 64(3):858–897, 2015.

[27] D. De Vos, A. Dzhurakhalov, S. Stijven, P. Klosiewicz, G. T. Beemster, and J. Broeckhove. Virtual Plant Tissue : Building Blocks for Next-Generation Plant Growth Simulation. *Frontiers in plant science*, 8(May):1–13, 2017.

[28] W. Dehnen and H. Aly. Improving convergence in smoothed particle hydrodynamics simulations without pairing instability. *Monthly Notices of the Royal Astronomical Society*, 425(2):1068–1082, 2012.

[29] J. Delile, M. Herrmann, N. Peyriéras, and R. Doursat. A cell-based computational model of early embryogenesis coupling mechanical behaviour and gene regulation. *Nature Communications*, 8:1–10, 2017.

[30] H. Downie, W. Otten, A. Spiers, T. Valentine, and D. LX. Transparent soil for imaging the rhizosphere. *PLoS One*, 7(9), 2012.

[31] J. Dumais, S. L. Shaw, C. R. Steele, S. R. Long, and P. M. Ray. An anisotropic-viscoplastic model of plant cell morphogenesis by tip growth. *International Journal of Developmental Biology*, 50(2-3):209–222, 2006.

[32] L. Dupuy, J. Mackenzie, and J. Haseloff. Coordination of plant cell division and expansion in a simple morphogenetic system. *Proceedings of the National Academy of Sciences of the United States of America*, 107(6):2711–2716, 2010.

[33] L. Dupuy, M. Mimault, D. Patko, V. Ladmiral, B. Ameduri, M. MacDonald, and M. Ptashnyk. Micromechanics of root development in soil. *Current opinion in genetics & development*, 51:18–25, 2018.

[34] L. Errera. Uber zellformen und seifenblasen. *Bot. Centralbl.*, 34:395–398, 1888.

[35] T. R. Faisal, N. Hristozov, T. L. Western, A. D. Rey, and D. Pasini. Computational study of the elastic properties of Rheum rhabarbarum tissues via surrogate models of tissue geometry. *Journal of Structural Biology*, 185(3):285–294, 2014.

[36] F. Federici, L. Dupuy, L. Laplaze, M. Heisler, and J. Haseloff. Integrated genetic and computation methods for in planta cytometry. *Nature Methods*, 9(5):483–485, 2012.

[37] C. Federrath, R. Banerjee, P. C. Clark, and R. S. Klessen. Modeling Collapse and Accretion in Turbulent Gas Clouds: Implementation and Comparison of Sink Particles in Amr and Sph. *The Astrophysical Journal*, 713(1):269–290, 2010.

[38] C. A. Felippa and E. Oñate. Stress, strain and energy splittings for anisotropic elastic solids under volumetric constraints. *Computers and Structures*, 81(13):1343–1357, 2003.

[39] M. D. Fuller. *The Application Of Smooth Particle Hydrodynamics To The Modelling Of Solid Materials*. PhD thesis, University of Leicester Engineering Department, July 2010.

[40] K. M. Furuta, E. Hellmann, and Y. Helariutta. Molecular Control of Cell Specification and Cell Differentiation During Procambial Development. *Annual Review of Plant Biology*, 65(1):607–638, 2014.

[41] A. Geitmann and J. K. E. Ortega. Mechanics and modeling of plant cell growth. *Trends in plant science*, l(9):467–478, 2009.

[42] P. Ghysels, G. Samaey, B. Tijskens, P. Van Liedekerke, H. Ramon, and D. Roose. Multi-scale simulation of plant tissue deformation using a model for individual cell mechanics. *Physical Biology*, 6(1), 2009.

[43] L. J. Gibson. The hierarchical structure and mechanics of plant materials. *Journal of the Royal Society Interface*, 9(76):2749–2766, 2012.

[44] R. A. Gingold and J. J. Monaghan. Smoothed particle hydrodynamics - Theory and application to non-spherical stars. *Monthly Notices of the Royal Astronomical Society*, 181:375–389, Nov. 1977.

[45] A. Goriely. *The mathematics and mechanics of biological growth*, volume 45. Springer, 2017.

[46] J. P. Gray, J. J. Monaghan, and R. P. Swift. SPH elastic dynamics. *Computer Methods in Applied Mechanics and Engineering*, 190(49-50):6641–6662, 2001.

[47] Y. Guo and J. S. Curtis. Discrete Element Method Simulations for Complex Granular Flows. *Annual Review of Fluid Mechanics*, 47(1):21–46, 2015.

[48] O. Hamant, M. G. Heisler, H. Jonsson, P. Krupinski, M. Uyttewaal, P. Bokov, F. Corson, P. Sahlin, A. Boudaoud, E. M. Meyerowitz, Y. Couder, and J. Traas. Developmental Patterning by Mechanical Signals in Arabidopsis. *Science*, 322(5908):1650–1655, dec 2008.

[49] T. Heck, B. Smeets, S. Vanmaercke, P. Bhattacharya, T. Odenthal, H. Ramon, H. Van Oosterwyck, and P. Van Liedekerke. Modeling extracellular matrix viscoelasticity using smoothed particle hydrodynamics with improved boundary treatment. *Computer Methods in Applied Mechanics and Engineering*, 322:515–540, 2017.

[50] W. Hu, W. Pan, M. Rakhsha, Q. Tian, H. Hu, and D. Negrut. A consistent multi-resolution smoothed particle hydrodynamics method. *Computer Methods in Applied Mechanics and Engineering*, 324:278–299, 2017.

[51] Y. Huang, Z. Dai, and W. Zhang. *Geo-disaster Modeling and Analysis: An SPH-based Approach.* Springer, 2014.

[52] M. R. I. Islam, S. Chakraborty, A. Shaw, and S. Reid. A Computational Model for Failure of Ductile Material under Impact. *International Journal of Impact Engineering*, 2017.

[53] O. E. Jensen and J. A. Fozard. Multiscale Models in the Biomechanics of Plant Growth. *Physiology*, 30(2):159–166, mar 2015.

[54] A. R. Jones, M. Forero-Vargas, S. P. Withers, R. S. Smith, J. Traas, W. Dewitte, and J. A. Murray. Cell-size dependent progression of the cell cycle creates homeostasis and flexibility of plant cell size. *Nature Communications*, 8:15060, 2017.

[55] G. W. Jones and S. J. Chapman. Modeling Growth in Biological Materials. *SIAM Review*, 54(1):52–118, 2012.

[56] H. C. P. Karunasena, W. Senadeera, Y. T. Gu, R. J. Brown, C. P. K. Helambage, W. Senadeera, Y. T. Gu, and R. J. Brown. A coupled SPH-DEM model for fluid and solid mechanics of apple parenchyma cells during drying. *Proceedings of the Eighteenth Australasian Fluid Mechanics Conference*, 2012.

[57] S. Kitsionas and A. Whitworth. Smoothed particle hydrodynamics with particle splitting, applied to self-gravitating collapse. *Monthly Notices of the Royal Astronomical Society*, 330(1):129–136, 2002.

[58] J. H. Kroeger, A. Geitmann, and M. Grant. Model for calcium dependent oscillatory growth in pollen tubes. *Journal of Theoretical Biology*, 253(2):363–374, 2008.

[59] E. Kuhl, A. Menzel, and P. Steinmann. Computational modeling of growth. A critical review, a classification of concepts and two new consistent approaches. *Computational Mechanics*, 32(1-2):71–88, 2003.

[60] D. Kwiatkowska. Structural integration at the shoot apical meristem: Models, measurements, and experiments. *American Journal of Botany*, 91(9):1277–1293, 2004.

[61] F. M. Lang, A. S. Iglesias, M. Antuono, and A. Colagrossi. Benefits of using a wendland kernel for free-surface flows. In *Proceedings of 6th ERCOFTAC SPHERIC workshop on SPH applications*, pages 30–37, 2011.

[62] A. Leroy, D. Violeau, M. Ferrand, L. Fratter, and A. Joly. A new open boundary formulation for incompressible SPH. *Computers and Mathematics with Applications*, 72(9):2417–2432, 2016.

[63] M. Liu and G. Liu. Smoothed particle hydrodynamics (sph): an overview and recent developments. *Archives of computational methods in engineering*, 17(1):25–76, 2010.

[64] W. T. Liu, P. N. Sun, F. R. Ming, and A. M. Zhang. Application of particle splitting method for both hydrostatic and hydrodynamic cases in SPH. *Acta Mechanica Sinica*, pages 1–26, 2017.

[65] A. C. Lloyd, S. Laura, E. Georgina, H. L. Katherine, M. James, C. Natalie, J. Rebecca, L. Sarah, P. Jonathan, D. Brian, Y. Davit, C. G. Bell, H. M. Byrne, L. A. C. Chapman, L. S. Kimpton, G. E. Lang, K. H. L. Leonard, J. M. Oliver, N. C. Pearson, R. J. Shipley, S. L. Waters,

J. P. Whiteley, B. D. Wood, and M. Quintard. Homogenization via formal multiscale asymptotics and volume averaging : How do the two techniques compare ? *Advances in Water Resources*, 62:178–206, 2013.

[66] C. Lloyd and H. Buschmann. Plant division: remembering where to build the wall. *Current Biology*, 17(24):R1053–R1055, 2007.

[67] M. Louveaux, J.-D. Julien, V. Mirabet, A. Boudaoud, and O. Hamant. Cell division plane orientation based on tensile stress in arabidopsis thaliana. *Proceedings of the National Academy of Sciences*, 113(30):E4294–E4303, 2016.

[68] L. B. Lucy. A numerical approach to the testing of the fission hypothesis. *Astronomical Journal*, 82:1013–1024, Dec. 1977.

[69] M. Marin-Riera, J. Moustakas-Verho, Y. Savriama, J. Jernvall, et al. Differential tissue growth and cell adhesion alone drive early tooth morphogenesis: An ex vivo and in silico study. *PLoS computational biology*, 14(2):1–26, 2018.

[70] D. A. Matoz-Fernandez, K. Martens, R. Sknepnek, J. L. Barrat, and S. Henkes. Cell division and death inhibit glassy behaviour of confluent tissues. *Soft Matter*, 13:3205–3212, 2016.

[71] V. Mironova, W. Teale, M. Shahriari, J. Dawson, and K. Palme. The Systems Biology of Auxin in Developing Embryos. *Trends in Plant Science*, 22(3):225–235, 2017.

[72] J. Monaghan. Smoothed Particle Hydrodynamics and Its Diverse Applications. *Annual Review of Fluid Mechanics*, 44(1):323–346, 2012.

[73] J. J. Monaghan. Smoothed particle hydrodynamics. *Annual review of astronomy and astrophysics*, 30:543–574, 1992.

[74] J. J. Monaghan. Smoothed particle hydrodynamics. *Reports on progress in physics*, 68(8):1703, 2005.

[75] M. Osorno and H. Steeb. Smoothed particle hydrodynamics modelling of poroelastic media. *PAMM*, 16(1):469–470, 2016.

[76] M. Osorno and H. Steeb. Smoothed particle hydrodynamics model of poroelasticity-fluid coupling. *PAMM*, 18(1):e201800448, 2018.

[77] A. Palyanov and S. Khayrulin. Sibernetic: A software complex based on the PCI SPH algorithm aimed at simulation problems in biomechanics. *Russian Journal of Genetics: Applied*, 5(6):635–641, 2015.

[78] A. Peaucelle. *Cell Wall Expansion: Case Study of a Biomechanical Process*, pages 139–154. Springer, 2018.

[79] A. Piatnitski and M. Ptashnyk. Homogenization of biomechanical models for plant tissues. *Multiscale Modeling & Simulation*, 15(1):339–387, 2017.

[80] D. J. Price, J. Wurster, T. S. Tricco, C. Nixon, S. Toupin, A. Pettitt, C. Chan, D. Mentiplay, G. Laibe, S. Glover, and et al. Phantom: A smoothed particle hydrodynamics and magnetohydrodynamics code for astrophysics. *Publications of the Astronomical Society of Australia*, 35:e031, 2018.

[81] P. Prusinkiewicz and A. Runions. Computational models of plant development and form. *New Phytologist*, 193(3):549–569, 2012.

[82] M. Ptashnyk and B. Seguin. The Impact of Microfibril Orientations on the Biomechanics of Plant Cell Walls and Tissues. *Bulletin of Mathematical Biology*, 78(11):2135–2164, 2016.

[83] M. K. Rausch, G. E. Karniadakis, and J. D. Humphrey. Modeling Soft Tissue Damage and Failure Using a Combined Particle/Continuum Approach. *Biomechanics and Modeling in Mechanobiology*, 16(1):249–261, 2017.

[84] J. Renner and H. Steeb. Modeling of fluid transport in geothermal research. *Handbook of Geomathematics*, pages 1443–1505, 2015.

[85] A.-L. Routier-Kierzkowska and A. Runions. Modeling plant morphogenesis: An introduction. In *Plant Biomechanics*, pages 165–192. Springer, 2018.

[86] P. Sahlin and H. Jönsson. A modeling study on how cell division affects properties of epithelial tissues under isotropic growth. *PloS One*, 5(7):e11750, 2010.

[87] V. Springel. The cosmological simulation code gadget-2. *Monthly Notices of the Royal Astronomical Society*, 364(4):1105–1134, 2005.

[88] E. Steudle. Water flow in plants and its coupling to other processes: An overview. In *Methods in enzymology*, volume 174, pages 183–225. Elsevier, 1989.

[89] B. Szigeti, P. Gleeson, M. Vella, S. Khayrulin, A. Palyanov, J. Hokanson, M. Currie, M. Cantarelli, G. Idili, and S. Larson. OpenWorm: an open-science approach to modeling Caenorhabditis elegans. *Frontiers in computational neuroscience*, 8(November):137, 2014.

[90] R. Vacondio, B. Rogers, P. Stansby, and P. Mignosa. Variable resolution for sph in three dimensions: Towards optimal splitting and coalescing for dynamic adaptivity. *Computer Methods in Applied Mechanics and Engineering*, 300:442–460, 2016.

[91] R. Vacondio, B. D. Rogers, P. K. Stansby, P. Mignosa, and J. Feldman. Variable resolution for SPH: A dynamic particle coalescing and splitting scheme. *Computer Methods in Applied Mechanics and Engineering*, 256:132–148, 2013.

[92] P. Van Liedekerke, M. Palm, N. Jagiella, and D. Drasdo. Simulating tissue mechanics with agent-based models: concepts, perspectives and some novel results. *Computational Particle Mechanics*, 2(4):401–444, 2015.

[93] P. Van Liedekerke, E. Tijskens, H. Ramon, P. Ghysels, G. Samaey, and D. Roose. Particle-based model to simulate the micromechanics of biological cells. *Physical Review E - Statistical, Nonlinear, and Soft Matter Physics*, 81(6), 2010.

[94] L. Verlet. Computer "Experiments" on Classical Fluids. I. Thermodynamical Properties of Lennard-Jones Molecules. *Physical Review*, 159(2):183–195, 1967.

[95] H. Wendland. Piecewise polynomial, positive definite and compactly supported radial functions of minimal degree. *Advances in Computational Mathematics*, 4(1):389–396, 1995.

[96] R. Winchenbach, H. Hochstetter, and A. Kolb. Infinite continuous adaptivity for incompressible sph. *ACM Transactions on Graphics (TOG)*, 36(4):102, 2017.

[97] J. Yan, X. Ni, and L. Yang. Robust cell size checkpoint from spatiotemporal positive feedback loop in fission yeast. *BioMed research international*, 2013, 2013.

[98] S. Yashiro. Application of particle simulation methods to composite materials: a review. *Advanced Composite Materials*, 26(1):1–22, 2017.

[99] S. Yoshida, P. B. de Reuille, B. Lane, G. W. Bassel, P. Prusinkiewicz, R. S. Smith, and D. Weijers. Genetic control of plant development by overriding a geometric division rule. *Developmental cell*, 29(1):75–87, 2014.

[100] J. J. Zhu, E. Steudle, and E. Beck. Negative pressures produced in an artificial osmotic cell by extracellular freezing. *Plant physiology*, 91(4):1454–1459, 1989.